Oxygen Surface Exchange at Grain Boundaries of Oxide Ion Conductors

Wonyoung Lee, Hee Joon Jung, Min Hwan Lee, Young-Beom Kim, Joong Sun Park, Robert Sinclair, and Fritz B. Prinz*

The role of grain boundaries on oxygen surface exchange in an oxide ion conductor is reported. Atomic-scale characterization of the microstructure and chemical composition near the grain boundaries of gadolinia-doped ceria (GDC) thin films show the segregation of dopants and oxygen vacancies along the grain boundaries using the energy dispersive spectroscopy in scanning transmission electron microscopy (STEM-EDS). Kelvin probe microscopy is employed to verify the charge distribution near grain boundaries and shows that the grain boundary is positively charged, indicating a high concentration of oxygen vacancies. AC impedance spectroscopy on polycrystalline GDC membranes with thin interfacial layers with different grain boundary densities at the cathodes demonstrated that the cells with higher grain boundary density result in lower electrode impedance and higher exchange current density. These experimental evidences clearly show that grain boundaries on the surface provide preferential reaction sites for facilitated oxygen incorporation into the GDC electrolyte.

1. Introduction

Fluorite-structured oxide materials such as yttria-stabilized zirconia (YSZ) and gadolinia-doped ceria (GDC) have been widely investigated as solid state electrolytes for electrochemical devices including solid oxide fuel cells (SOFCs),[1] oxygen gas sensors,[2] oxygen pumps,[3] and electrochemical reactors.[4] YSZ is one of the most commonly used oxide ion conductors for SOFCs because of its excellent chemical stability at elevated temperatures. However, the high operating temperature of 800–1000 °C to attain the desired range of ionic conductivity and high activation energy barrier for oxide ion diffusion often limit applications. Therefore, extensive research has been conducted to lower the operating temperature by fabricating thin film structures and/or by replacing YSZ with other materials such as rare-earth-doped ceria, which shows higher oxide ion conductivity. For example, GDC has shown the higher ionic conductivity at 600–800 °C with the lower activation energies than those of YSZ.[5–7] GDC has the same fluorite structure as YSZ. Doping of gadolinia (Gd_2O_3) into fluorite-structured ceria (CeO_2) lattice induces oxide ion vacancies, in which oxide ions are incorporated and transported. Although GDC turns into a mixed conductor at elevated temperatures in reducing environment, it conducts only oxide ions below 500 °C.[8]

Fabrication of thin electrolytes generally forms polycrystalline films, and many of the important properties of the polycrystalline materials used in these applications highly depend on the structure and composition of grain boundaries. For example, ionic conductivity across grain boundaries in oxide ion conductors is well known to be several orders of magnitude below the bulk conductivity.[9–11] The grain boundary resistivity was found to be influenced by dopant segregation and the segregation level varied with grain size.[12] Thus, grain boundaries often dominate the overall resistivity and, in turn, the device performance. Grain boundaries become especially important in thin film devices that have a high density of grain boundaries as well as a large surface-to-volume ratio. However, the role of grain boundaries in surface exchange kinetics of oxygen on an electrolyte surface is not well-understood, especially in the low temperature regime, i.e., below 500 °C, where surface kinetics usually dominates ionic transport processes.[13–15] For the development of future applications, it is essential to develop a fundamental understanding of the structure and composition at grain boundaries and their effect on device performance.

In this study, we report the effect of local distribution of chemical composition in the vicinity of grain boundaries on the oxygen incorporation reactions. To investigate the microstructure and chemical composition at grain boundaries, we

Dr. W. Lee,[+] Dr. Y.-B. Kim, J. S. Park, Prof. F. B. Prinz
Nanoscale Prototyping Laboratory
Department of Mechanical Engineering
Stanford University
Stanford, CA 94305, USA
E-mail: leewy@stanford.edu
H. J. Jung, Prof. R. Sinclair, Prof. F. B. Prinz
Department of Materials Science and Engineering
Stanford University
Stanford, CA 94305, USA
Dr. M. H. Lee
Department of Materials Science and Engineering
Seoul National University
Seoul, 151-742, South Korea
[+] Present address: Laboratory of Electrochemical Interfaces, Department of Nuclear Science and Engineering, Massachusetts Institute of Technology, Cambridge, MA 02139, USA, E-mail: leewy@mit.edu

DOI: 10.1002/adfm.201101996

analyzed the nanocrystalline GDC thin film using energy dispersive spectroscopy in scanning transmission electron microscopy (STEM-EDS).[16] We also employed Kelvin probe microscopy (KPM)[17] for obtaining local charge distribution maps near grain boundaries to validate the analysis by STEM-EDS. The role of grain boundaries on the oxide surface in oxygen incorporation was further investigated by AC impedance spectroscopy to extract exchange current density, which has direct bearings on the performance of solid oxide fuel cells.

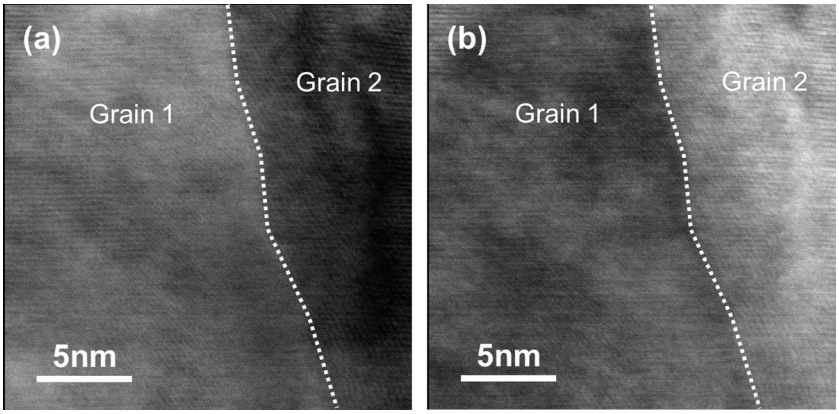

Figure 2. STEM images of GDC grain boundaries where STEM-EDS spectra were acquired. a) Bright-field image and b) dark-field image.

2. Results and Discussion

2.1. STEM-EDS Analysis

Figure 1 shows a high-resolution transmission electron microscopy (TEM) image of the polycrystalline GDC grain boundaries. In this fluorite-structured material, the bright dots in the image correspond to the positions of the Ce/Gd columns, i.e., the cation sublattice. Since the atomic radii of Ce^{4+} and Gd^{3+} are very similar to each other, 0.97 Å for Ce^{4+} and 1.05 Å for Gd^{3+},[18] it was difficult to distinguish the occupancy of Gd^{3+} on the Ce^{4+} lattice sites directly from the image. Furthermore, the oxygen atoms, which are located between the cation columns, are not visible in this TEM image because they have a much smaller atomic number than Ce and Gd.

Since the local distribution of atomic species, such as the Gd^{3+} ions and the oxygen vacancies at the grain boundaries, cannot be achieved directly from the TEM analysis, we acquired STEM-EDS spectra as a function of position near a grain boundary region. **Figure 2** shows the bright-field and dark-field STEM images of GDC grain boundary where STEM-EDS spectra were acquired. The dashed line represents the grain boundary between two grains.

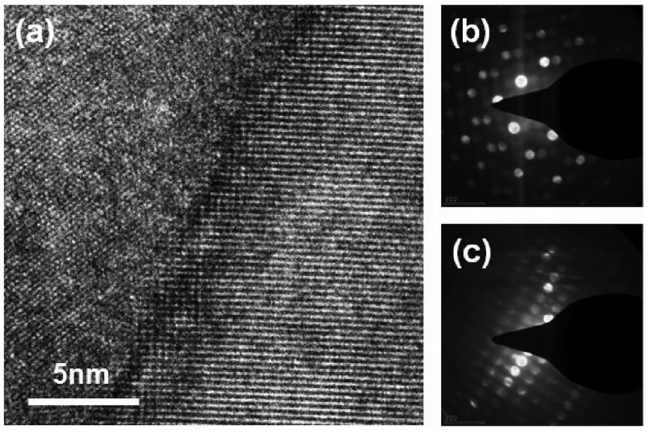

Figure 1. a) High-resolution TEM image of GDC grain boundaries. Convergent beam electron diffraction patterns of b) the left grain, which is close to <110> zone, and c) the right grain, which is close to <211> zone.

Figure 3 shows EDS point spectra measured at a spot directly on a grain boundary region and another spot more than 10 nm away from the grain boundary. They were obtained with a probe size of less than 2 nm, an energy resolution of 134 eV, and an acquisition time of 10 s for each location. Although we cannot confirm different chemical composition at each spot, the intensity ratio of two elements can provide qualitative information about the differences in the chemical composition. As shown in Figure 3, the intensities of Ce L peaks from the two spots appear similar to each other. However, the intensity of Gd L peaks is higher and that of O K peak is lower at the grain boundary region, i.e., the atomic ratio of Gd/Ce is higher but O/Ce is lower at grain boundaries. This result suggests that the higher concentration of Gd^{3+} ions and lower concentration of O^{2-} ions along the grain boundary region.

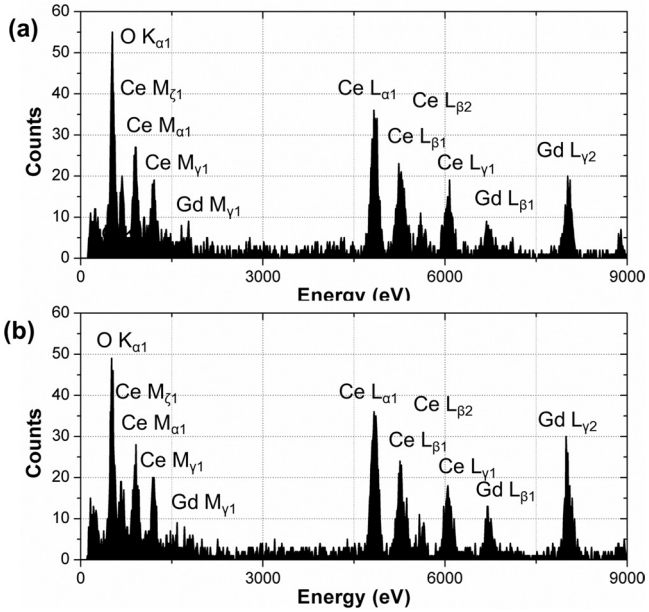

Figure 3. STEM-EDS spectra obtained a) more than 10 nm away from grain boundaries and b) at grain boundaries.

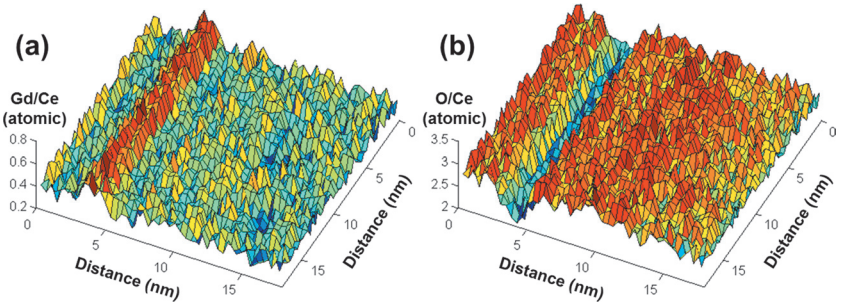

Figure 4. 3D concentration ratio maps near grain boundaries. a) Gd/Ce ratio and b) O/Ce ratio. The map contains 46 pixels × 46 pixels over 18 × 18 nm^2. The acquisition time for each point was 10 s.

In an effort to further elucidate the differences in the chemical composition between the two regions, an elemental mapping was acquired near the area where the point measurement was performed. A set of STEM-EDS spectra was acquired in an area of 20 × 20 nm^2 near a grain boundary. The absolute intensity profiles of Ce $L_{\alpha1}$, Gd $L_{\gamma2}$, and O $K_{\alpha1}$ shells were converted to atomic fraction considering detector correction factors and k-factors of each element, which were calculated using a TEM computer software (Supporting Information, Table S1).

Figure 4 shows atomic ratio maps of Gd/Ce and O/Ce acquired in the predefined area. The distinct protrusion in a Gd/Ce map and depression in an O/Ce map correspond to the grain boundary shown in Figure 2. The maps in Figure 4a,b clearly show an increase of the Gd/Ce ratio and a decrease of the O/Ce ratio along the grain boundary, indicating a segregation of Gd^{3+} ions and a depletion of O^{2-} ions along the grain boundary region. Since the depletion of O^{2-} ions can be considered equivalently as the accumulation of oxygen vacancies, the maps indicate that both Gd^{3+} ions and oxygen vacancies were segregated toward the grain boundary.

Figure 5a,b show the atomic ratio profiles of Gd/Ce and O/Ce along the line perpendicular to the grain boundary. Each point was obtained by averaging all the data parallel to the grain boundary in the maps shown in Figure 4. The uncertainty level of each ratio profile was found to be less than 5% from a curve fitting error calculation. The composition of GDC samples was measured to be $Gd_{0.29}Ce_{0.71}O_{1.92}$ from an X-ray photoelectron spectroscopy (XPS) analysis over a large area of 100 × 100 μm^2, and the corresponding values of Gd/Ce and O/Ce are indicated in red lines in Figure 5a,b. Although both Gd/Ce and O/Ce ratios were substantially different from the values measured by the XPS at the grain boundary regions, they converged to similar values at locations far away from the grain boundary. Thus, we considered the atomic ratios measured at locations far away from the grain boundary as the bulk value. Therefore, based on the atomic ratio profiles, we can obtain the composition at the bulk and the grain boundary as $Gd_{0.30 \pm 0.02}Ce_{0.70 \pm 0.02}O_{1.82 \pm 0.11}$ and $Gd_{0.36 \pm 0.06}Ce_{0.64 \pm 0.05}O_{1.41 \pm 0.17}$, respectively. The Gd/Ce ratio increases from 0.4 to 0.6, while the O/Ce ratio decreases from 2.7 to 2.2 towards the grain boundaries. This dopant segregation at the grain boundary is consistent with previous observations using molecular dynamics (MD) Monte Carlo (MC) simulation,[19] low energy loss ion scattering (LEIS),[20] and electron energy loss spectroscopy (EELS) in STEM,[21] which are summarized in **Table 1**. The discrepancy in the dopant enrichment factor, which is the atomic ratio of dopants between the grain boundary and the bulk, is probably due to the difference in the measurement accuracy, lateral resolution of each method, and the sintering/annealing conditions. Most of samples from the literature are sintered or annealed at high temperature, up to 2000 K, but the sample used in this study was annealed only at 650 °C. Atomic ratio profile of Gd/Ce in this study shows no clear indication of dopant depletion next to the grain boundary core, which was also indicated in the MD-MC simulation.[19] However, the intensive dopant segregation within 1.5–2.0 nm from the grain boundaries agrees well with the STEM-EELS and the LEIS

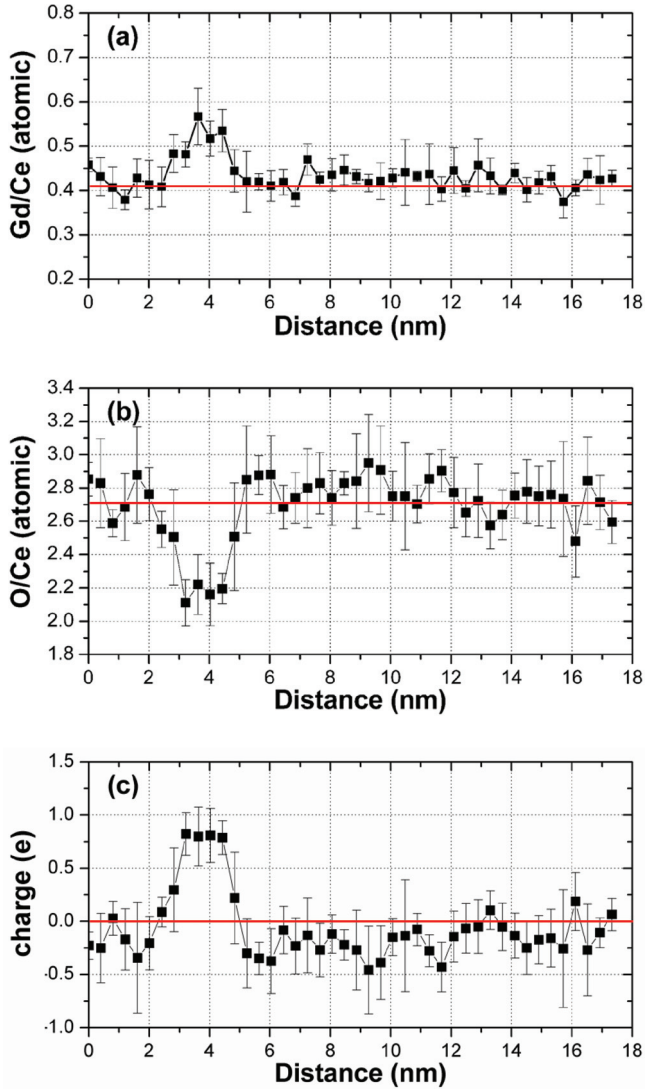

Figure 5. Line profiles of a) Gd/Ce ratio, b) O/Ce ratio, and c) calculated charge. Each profile was drawn along the line perpendicular to the grain boundaries. The red lines represent the values from XPS analysis.

Table 1. Gd/Ce atomic ratio in the bulk and at the grain boundaries using MD-MC simulation, LEIS, and STEM-EELS in $Gd_{0.2}Ce_{0.8}O_{2-x}$.

Method	Bulk	Grain boundary	Enrichment factor	Temperature [K]	Ref.
MD-MC	0.18	0.68	3.1	2000	[19]
LEIS	0.24 ± 0.3	≈1	4.2	1873	[20]
STEM-EELS	0.42 ± 0.08	0.69 ± 0.15	1.6	1773–1873	[21]
STEM-EDS	0.43 ± 0.02	0.57 ± 0.06	1.4	923	This work

measurements and the MD-MC simulation. In addition, the dopant segregation at grain boundaries is also observed in YSZ theoretically[19] and experimentally,[21] suggesting that this non-stoichiometry may be generic to grain boundaries of fluorite-structured oxide ion conductors.

Figure 5c shows a charge profile along the line perpendicular to the grain boundary. We assumed the valence states of Ce, Gd, and O are 4+, 3+, and 2–, respectively, because those are the most stable valence states. Combined with concentration ratio profiles, the width of the grain boundary was estimated to be ≈3 nm (or ≈1.5 nm per each grain), which is consistent with other observations and calculations.[19–23] In the grain boundary region, Gd^{3+} ions and oxygen vacancies were segregated. However, the segregation level of Gd^{3+} ions was insufficient to fully charge balance the segregation of oxygen vacancies, resulting in a positive net potential in the region. Since not all charges were balanced in the grain boundary region, the remaining negative charges should reside in the bulk region. This may be because the temperature and duration for the annealing process were not high and long enough to enable the system to reach a thermodynamic equilibrium. Otherwise, the bulk region would have been perfectly neutral. In the bulk region, there is a slight segregation of O^{2-} ions, resulting in a slight negative net potential. These negative charges complete the neutrality of the film as a whole, compensating the positive charge in the grain boundary region. However, due to the much larger area of the bulk region, the net charge per area (or per profile length) is virtually neutral and thus the chemical composition is consistent with the XPS measurement. From the concentration profiles, the potential difference between the grain boundary and the bulk was calculated to be 60–80 mV, which is consistent with the charge profile that shows the positive grain boundary.

2.2. KPM Analysis

In order to confirm the charge distribution near grain boundaries, we performed surface potential measurements on the GDC thin film using the KPM. **Figure 6** shows the topography and the corresponding surface potential map acquired on the thin GDC film. The grain size was 20–50 nm in diameter and the root-mean-square (RMS) roughness in an area of 1 × 1 μm^2 was 3.5 nm. Due to the finite tip apex and the resulting topological convolution between the tip and the sample surface, it is often difficult to observe the true electrical properties of the sample, especially when the targeted lateral resolution is similar to or less than the tip apex dimension. In an effort to circumvent the artifact, a customized KPM was employed to obtain the surface potential map on the GDC film.[24] It is clearly shown that the surface potential along the grain boundary region was higher than that measured at the regions far from the grain boundaries. This indicates that grain boundary regions have positive net charges, which is consistent with STEM-EDS analysis, and other experimental evidences reporting an inherently positive grain boundary.[11–26] The potential difference between grain boundaries and grains was 100–150 mV. From the classical Mott–Schottky barrier model[23] and the impedance spectroscopy,[22] the space charge potential, which represents the potential difference between the grain boundary and the bulk, was calculated to be approximately 100–200 mV, which is consistent with the KPM measurements. The width of positively charged grain boundaries appeared to be 5–10 nm in the surface potential map, which is larger than the width observed form the STEM-EDS analysis. However, considering that KPM uses the capacitive interaction between the tip and the sample surface, which is proportional to the inverse of the square of the tip–sample separation, the measured width of the charged layer by the KPM can be larger than the actual feature width.[27]

2.3. EIS Analysis

Through the STEM-EDS and KPM analyses, it became clear that oxygen vacancies favor to congregate along the grain boundaries, resulting in a positive net potential. During a low-temperature SOFC operation, the oxygen reduction reaction at the cathode interface is known to be the rate-limiting step determining the overall performance of the cell. Since the oxygen vacancy is basically the charge incorporation site for the cathodic reaction, the grain boundaries, which bear a high concentration of oxygen vacancy, should have the key enhancing the surface kinetics. To further confirm the active role of the grain boundaries in

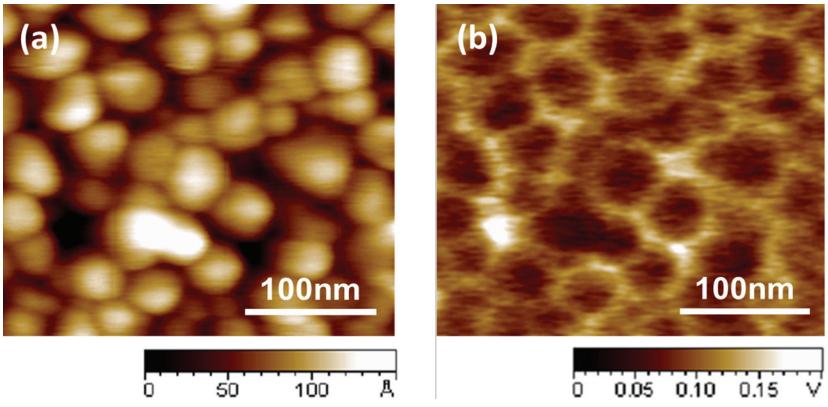

Figure 6. AFM images on the GDC thin film. a) Topography and b) corresponding surface potential map using the customized KPM.

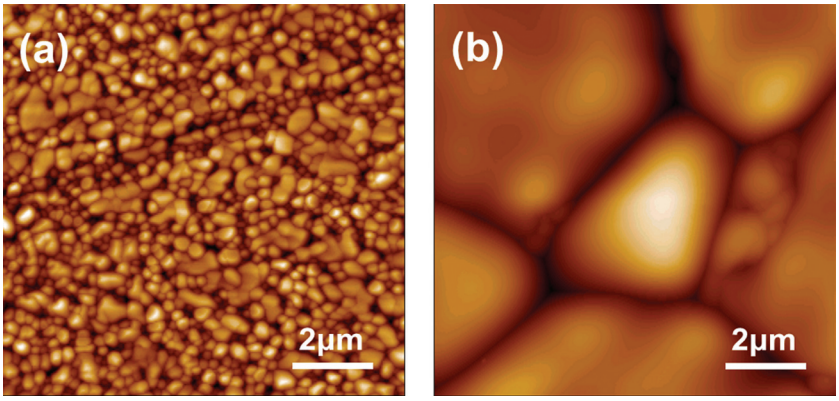

Figure 7. AFM topographies of GDC surface layers annealed at a) 1100 °C and b) 1400 °C.

enhancing the oxygen incorporation, additional experiments were conducted. 250–300 nm thick GDC layers using pulsed laser deposition (PLD) was added on top of two separate 200 μm thick polycrystalline GDC substrates. After the addition of GDC layers to the cathode side, the two samples were annealed at two different temperatures, 1100 and 1400 °C, in air for 10 h. The resulting size of grains in the two samples became considerably different form each other, as shown in **Figure 7**. Before adding GDC layers by PLD, we confirmed that neither the surface morphology nor the grain size of underlying polycrystalline GDC samples changed noticeably upon annealing in this temperature range. Therefore, each sample had the same grain structure in the bulk as well as at the anode side, but the different grain structure at the cathode surface.

After a deposition of porous platinum electrodes by DC sputtering, electrode impedance was measured using electrochemical impedance spectroscopy (EIS) at 300, 350, 400, and 450 °C under different DC bias values with regard to reference electrode connected to anode side. The anode and cathode were exposed to pure dry hydrogen and ambient air, respectively. The detailed information of the measurement setup is described earlier.[28] **Figure 8** shows a representative Nyquist plot measured on the sample annealed at 1100 °C with different DC biases. The measurement was carried out at 350 °C. The low frequency and high frequency arcs in the Nyquist plot are known to be originated from electrode processes and electrolyte impedances,[22,29,30] respectively. As expected, the size of high frequency arc was independent of the DC bias magnitude, indicating that this arc is

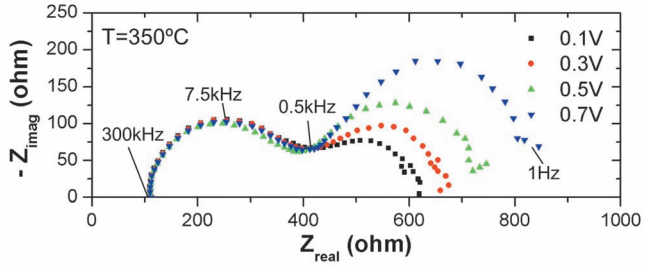

Figure 8. Nyquist plot of a sample annealed at 1100 °C under different DC bias with respect to reference electrode. Measurements were carried out at 350 °C with pure dry H_2 at the anode and ambient air at the cathode.

associated with charge transport through the GDC electrolyte, i.e., the diffusion of oxygen ions in the bulk. However, the size of the low frequency arc varied with DC bias values, confirming that the low frequency arc came from electrode processes. It is frequently reported that cathode reaction kinetics is much slower than that of anode reaction in SOFCs,[28,31,32] and the anode contribution to the total electrode impedance is usually considered as negligible, especially when measured across the electrolyte (out-of-plane) at low temperature. Therefore, the variation in the low frequency arc is due to the difference in the surface reaction at the cathode.[33,34]

Figure 9a shows the Faradaic impedance of the cathode reaction of the two samples, which were extracted from a numerical fitting of the low frequency arcs. The

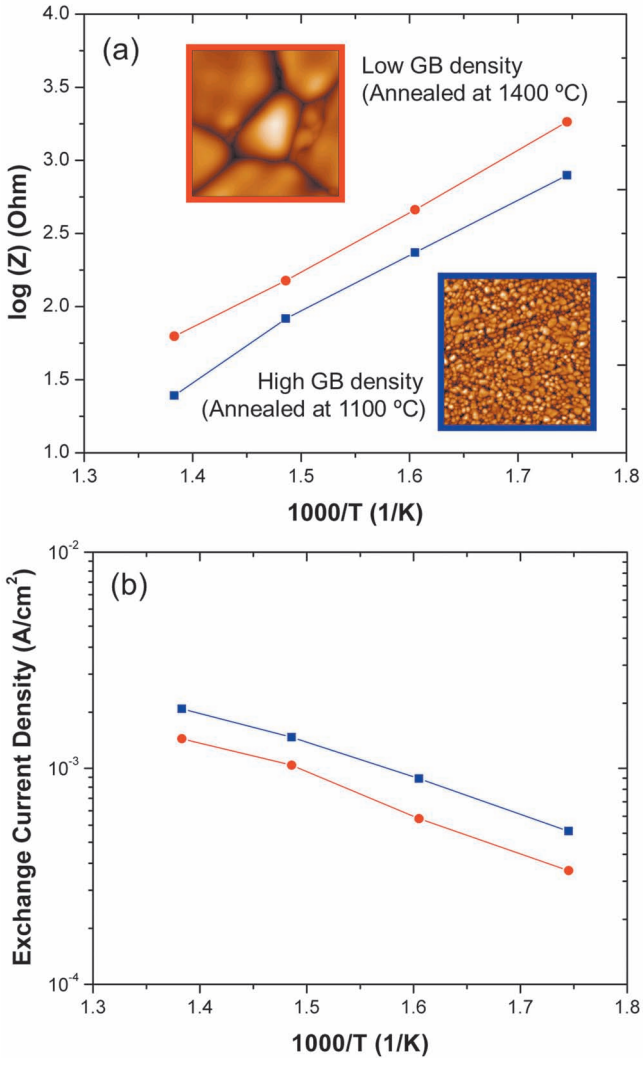

Figure 9. AC impedance spectroscopy of samples post-annealed at 1100 °C (blue squares) and 1400 °C (red circles) measured at varied temperatures. a) Cathodic impedance and b) exchange current density.

equivalent circuit for the fitting was comprised of two parallel resistance-capacitances (RC) and another resistance in series. EIS analysis showed that the cathodic impedance of the sample annealed at 1100 °C (with higher grain boundary density) was lower than that of the sample annealed at 1400 °C (with lower grain boundary density) in the temperature windows of observation. The trend was observed under given DC biases and temperatures. In addition, the values of the exchange current densities at each temperature were plotted in Figure 9b. The exchange current density is indicative of the rate of exchange between reactants and products at equilibrium, which is crucial for the performance of fuel cells.[35] The exchange current density of the sample with higher grain boundary density was substantially higher than that with lower grain boundary density at given measurement temperatures. This confirms the active role of grain boundaries for oxygen incorporation within the temperature range studied.

We also examined other parameters that might affect the cathodic impedance: the surface roughness and the chemical composition of the surface layer. The higher surface roughness can provide additional sites for surface reactions, which reduces the cathodic impedance. The change in the chemical composition of the surface layer deposited by PLD can also affect the surface reaction rate. An AFM topography scan in an area of 10×10 μm^2 revealed that the RMS roughness were 14 and 38 nm, and the actual surface areas were 102.4 and 100.6 μm^2 for the sample annealed at 1100 and 1400 °C, respectively. As shown here, there were no significant difference between the two samples in terms of the surface roughness and surface area. It was confirmed that there was no noticeable difference in the chemical composition of the two samples through the XPS analysis (Supporting Information, Figure S1). In addition to the electrolyte surface, we examined the microstructure of the Pt electrode, which can be affected by the underlying substrate.[36] Oxygen can penetrate preferably through Pt grain boundaries, which leads to lower cathodic impedance. An AFM topography scan of the Pt electrode revealed that the grain size were 30–50 nm for both samples with no difference. Scanning electron microscopy was also employed to investigate the surface morphologies in a larger area, but there was no noticeable difference between samples. With the deposition conditions used in this study, the microstructure of the Pt electrodes was not affected by the underlying substrate, yielding the consistent porous structures. These results suggest that the observed enhancement in the surface reactions is not caused by the change in the surface geometry or the chemical composition of the additional electrolyte layer and electrode.

3. Conclusions

A set of atomic-scale characterizations on the chemical composition and charge distribution has been performed near grain boundary region of nanocrystalline GDC thin films. The combination of STEM-EDS and KPM techniques has revealed segregation of Gd^{3+} ions and depletion of O^{2-} ions or segregation of dopants and oxygen vacancies in the grain boundary region. This dopant segregation partially compensated for the oxygen vacancy segregation, but the level of dopant segregation was insufficient to fully charge balance oxygen vacancies, resulting in a positive net potential in the grain boundary region. Subsequent EIS analysis of cathodic impedance on polycrystalline GDC samples with an interfacial layer at their cathodic interfaces with different grain boundary density has revealed that the interfacial layer with higher grain boundary density resulted in a lower cathodic impedance, indicating that grain boundaries are active reaction sites for oxygen incorporation. The pronounced role of grain boundaries was further supported by the higher exchange current density with the higher grain boundary density. This series of independent experimental results clearly shows that grain boundaries on the surface provide preferential reaction sites for facilitated oxygen incorporation into the GDC electrolyte. Recent work using secondary ion mass spectroscopy and EIS on YSZ and yttria-doped ceria[34,37] substantiates the enhanced oxygen incorporation into the electrolytes through grain boundaries on the electrolyte surface, suggesting that this active role of grain boundaries for oxygen incorporation is not specifically limited to GDC, but may be general characteristic of fluorite-structured cathode materials of SOFCs. These results have significant implications in designing electrolyte surfaces for improved surface exchange kinetics, and consequently enhanced device performance, especially at low temperatures.

4. Experimental Section

Thin Film Processing: Nanocrystalline GDC films were prepared by DC sputtering using $Gd_{0.2}Ce_{0.8}$ alloy target (Kurt Lesker Co.). These alloy films with thickness of 100 nm were oxidized in air at 650 °C for 5 h.[38,39] The grain sizes were within the range of 20–50 nm. Chemical composition was analyzed by a PHI Versa Probe monochromatized XPS spectrometer (Physical Electronics) with Al (Kα) radiation (1486 eV). The resulting spectra showed that the GDC films were composed of 9.9% Gd, 24.3% Ce, and 65.8% O with no impurities, such as silicon, within the sensitivity limit of the spectrometer (<0.1 at%). Silicon is an undesirable impurity in GDC that is known to potentially influence the chemical and electrical properties of grain boundaries. For PLD fabrication of GDC thin films, a sintered $Gd_{0.2}Ce_{0.8}O_{2-x}$ pellet (Kurt J. Lesker) was used as the target material. A Lambda Physik 248 nm KrF excimer laser with an energy density of 3.0 J cm^{-2} per pulse was used to ablate the target. During deposition, the substrate temperature was 500 °C, and the pressure of background oxygen was 30 mTorr. After deposition, samples were cooled under an oxygen pressure of 200 Torr for over 1 h. The deposition rate was ≈0.2 Å per pulse. The distance between the target and the substrate was set as 50 mm.

Pt thin films with thicknesses of 50–60 nm were deposited by DC sputtering. The target (purity >99.99 at%, Kurt J. Lesker) was used for deposition after surface cleaning of a plasma power of 50 W for 30 s. After pumping to a base pressure of 1×10^{-6} Torr, the depositions were carried out in 8×10^{-2} Torr of Ar with a plasma power of 50 W at room temperature. All samples used in this study were loaded together for deposition to eliminate the variation in thickness and uniformity among samples. Pt electrodes deposited on GDC samples were used in the as-deposited state without further annealing.

STEM-EDS Analysis: Samples with a thickness of 40–50 nm were prepared for TEM analysis using a focused ion beam (FIB, FEI Strata 235DB dual-beam FIB/SEM) lift-out Omniprobe technique with a Ga ion beam at 30 keV. Cross-sectional bright-field TEM images and convergent beam electron diffraction (CBED) patterns were taken by an FEI Tecnai G^2 F20 X-TWIN operated at an accelerating voltage of 200 kV. The same microscope was used for STEM analysis at an accelerating voltage of 200 kV and a beam current of 1 nA with extraction voltage of 4.2 kV, a gun lens of 6, and a spot size of 9. EDS spectra were analyzed using

background correction method with an energy resolution of 134 eV and a standard software, FEI TEM Imaging and Analysis (TIA).

KPM Analysis: A commercial AFM system (PicoPlus II, Molecular Imaging) was used for surface potential measurement with additional circuits to perform KPM. The tips used were Pt-coated silicon tips (PPP-NCHPt, Nanosensors) with a radius of 40–50 nm and resonance frequency of ≈63 kHz. Commercial RF lock-in amplifiers (SR830 DSP, SR844 RF, Stanford Research System) and custom-built circuitry were used for KPM feedback. For the surface potential measurement, we have used the customized KPM setups to minimize the artifacts from the tip-surface topological convolution effect, and detailed information can be found elsewhere.[24] Before the surface potential measurements, samples were heated at 200 °C for more than 1 h to eliminate a water layer absorbed on the surface, which could influence the surface potential measurements.[39,40]

EIS Analysis: EIS measurements were made with a Gamry FAS2 Femtostat system at 300, 350, 400, and 450 °C in the frequency range from 300 kHz to 0.1 Hz with an AC signal amplitude of 50 mV. The EIS results were analyzed and fitted to the spectra using Z-plot software based on complex nonlinear least-squares fitting method. Details of sample setups including gas feedings and substrate heating were described previously.[28,41,42]

Supporting Information

Supporting Information is available from the Wiley Online Library or from the author.

Acknowledgements

The authors thank the members of the Nanoscale Prototyping Laboratory for their support and discussions. In particular, the authors thank Dr. Turgut M. Gür for his insights and assistance. H.J.J., R.S., and F.B.P. acknowledge support by the US Department of Energy, Office of Science, Office of Basic Energy Sciences under DOE-EFRC: CNEEC (Award No. DESC0001060). J.S.P. was partially supported by a Samsung Scholarship.

Received: August 23, 2011
Revised: November 14, 2011
Published online: December 20, 2011

[1] S. P. S. Badwal, K. Foger, *Mater. Forum* **1997**, *21*, 183.
[2] T. Bak, J. Nowotny, M. Rekas, C. C. Sorrell, *MRS Bull.* **2001**, *26*, 435.
[3] F. T. Ciacchi, S. P. S. Badwal, *J. Austr. Ceram. Soc.* **1998**, *34*, 130.
[4] B. C. H. Steele, I. Kelly, H. Middleton, R. Rudkin, *Solid State Ionics* **1998**, *1547*, 28.
[5] B. C. H. Steele, *Solid State Ionics* **1995**, *75*, 157.
[6] J. B. Goodenough, *Annu. Rev. Mater. Res.* **2003**, *33*, 91.
[7] X.-D. Zhou, W. Huebner, I. Kosacki, H. U. Anderson, *J. Am. Ceram. Soc.* **2002**, *85*, 1757.
[8] Q. X. Fu, W. Zhang, R. R. Peng, D. K. Peng, G. Y. Meng, B. Zhu, *Mater. Lett.* **2002**, *53*, 186.
[9] C. A. Leach, P. Tanev, B. C. H. Steele, *J. Mater. Sci. Lett.* **1986**, *5*, 893.
[10] M. Aoki, Y.-M. Chiang, I. Kosacki, J. R. Lee, H. L. Tuller, Y. P. Liu, *J. Am. Ceram. Soc.* **1996**, *79*, 1169.
[11] X. Guo, J. Maier, *J. Electrochem. Soc.* **2001**, *148*, E121.
[12] J.-S. Lee, D.-Y. Kim, *J. Mater. Res.* **2001**, *16*, 2739.
[13] Z. Shao, S. M. Haile, *Nature* **2004**, *431*, 170.
[14] A. Atkinson, S. Barnett, R. J. Gorte, J. T. S. Irvine, A. J. McEvoy, M. Mogensen, S. C. Singhal, J. Vohs, *Nat. Mater.* **2004**, *3*, 17.
[15] J. Maier, *Phys. Chem. Chem. Phys.* **2009**, *11*, 3011.
[16] D. B. Williams, C. B. Carter, *Transmission Electron Microscopy: A Textbook for Materials Science*, Springer, New York **1998**.
[17] M. Nonnenmacher, M. P. O'Boyle, H. K. Wickramasinghe, *Appl. Phys. Lett.* **1991**, *58*, 2921.
[18] T. S. Zhang, J. Ma, L. B. Kong, S. H. Chan, P. Hing, J. A. Kilner, *Solid State Ionics* **2004**, *167*, 203.
[19] H. B. Lee, F. B. Prinz, W. Cai, *Acta Mater.* **2010**, *58*, 2197.
[20] P. J. Scanlon, R. A. M. Bink, F. P. F. van Berkel, G. M. Christie, L. J. van IJzendoorn, H. H. Brongersma, R. G. van Welzenis, *Solid State Ionics* **1998**, *112*, 123.
[21] Y. Lei, Y. Ito, N. D. Browning, T. J. Mazanec, *J. Am. Ceram. Soc.* **2001**, *85*, 2359.
[22] H. J. Avila-Paredes, K. Choi, C.-T. S. Chen, S. Kim, *J. Mater. Chem.* **2009**, *19*, 4837.
[23] X. Guo, R. Waser, *Prog. Mater. Sci.* **2006**, *51*, 151.
[24] M. Lee, W. Lee, F. B. Prinz, *Nanotechnology* **2006**, *17*, 3728.
[25] A. Tschöpe, *Solid State Ionics* **2001**, *139*, 267.
[26] S. Kim, J. Maier, *J. Electrochem. Soc.* **2002**, *149*, J73.
[27] Y. Shen, M. Lee, W. Lee, D. M. Barnett, P. M. Pinsky, F. B. Prinz, *Nanotechnology* **2008**, *19*, 035710.
[28] H. Huang, M. Nakamura, P. Su, R. Fasching, Y. Saito, F. B. Prinz, *J. Electrochem. Soc.* **2007**, *154*, B20.
[29] E. Barsoukov, J. R. Macdonald, *Impedance Spectroscopy: Theory, Experiment and Applications*, 2nd ed., John Wiley & Sons, Hoboken, NJ **2005**.
[30] H. L. Tuller, S. J. Litzelman, W. C. Jung, *Phys. Chem. Chem. Phys.* **2009**, *11*, 3023.
[31] S. Souza, S. J. Visco, L. C. De Jonghe, *Solid State Ionics* **1997**, *98*, 57.
[32] S. C. Singhal, K. Kendall, *High Temperature Solid Oxide Fuel Cells: Fundamentals, Design and Applications*, Elsevier, Oxford, UK **2003**.
[33] T. P. Holme, R. Pornprasertsuk, F. B. Prinz, *J. Electrochem. Soc.* **2010**, *157*, B64.
[34] J. H. Shim, J. S. Park, T. P. Holme, K. Crabb, W. Lee, Y. B. Kim, X. Tian, T. M. Gür, F. B. Prinz, *Acta Mater.* **2012**, *60*, 1.
[35] R. O'Hayre, S.-W. Cha, W. Colella, F. B. Prinz, *Fuel Cell Fundamentals*, John Wiley & Sons, Hoboken, NJ **2006**.
[36] T. Ryll, H. Galinski, L. Schlagenhauf, P. Elser, J. L. M. Rupp, A. Bieberle-Hutter, L. J. Gauckler, *Adv. Funct. Mater.* **2011**, *21*, 565.
[37] Y. B. Kim, J. S. Park, T. M. Gur, F. B. Prinz, *J. Power Sources* **2011**, *196*, 10550.
[38] H. Huang, T. M. Gür, Y. Saito, F. B. Prinz, *Appl. Phys. Lett.* **2006**, *89*, 143107.
[39] W. Lee, M. Lee, Y.-B. Kim, F. B. Prinz, *Nanotechnology* **2009**, *20*, 445706.
[40] S. V. Kalinin, D. A. Bonnell, *Nano Lett.* **2004**, *4*, 555.
[41] J. H. Shim, C.-C. Chao, H. Huang, F. B. Prinz, *Chem. Mater.* **2007**, *19*, 3850.
[42] P.-C. Su, C.-C. Chao, J. H. Shim, R. Fasching, F. B. Prinz, *Nano Lett.* **2008**, *8*, 2289.